Fast and Reliable Resampling Detection by Spectral Analysis of Fixed Linear Predictor Residue

Matthias Kirchner
Institute for System Architecture
Technische Universität Dresden
01062 Dresden, Germany
matthias.kirchner@inf.tu-dresden.de

ABSTRACT

This paper revisits the state-of-the-art resampling detector, which is based on periodic artifacts in the residue of a local linear predictor. Inspired by recent findings from the literature, we take a closer look at the complex detection procedure and model the detected artifacts in the spatial and frequency domain by means of the variance of the prediction residue. We give an exact formulation on how transformation parameters influence the appearance of periodic artifacts and analytically derive the expected position of characteristic resampling peaks. We present an equivalent accelerated and simplified detector, which is orders of magnitudes faster than the conventional scheme and experimentally shown to be comparably reliable.

Categories and Subject Descriptors

I.4.m [**Image Processing**]: Miscellaneous

General Terms

Algorithms, Security

Keywords

digital image forensics, tamper detection, resampling detection, predictor residuum, periodic artifacts

1. INTRODUCTION

Over the past years, research on digital image forensics and tamper detection has become a hot topic in the multimedia security community [12]. A wide distribution of low-cost digital imaging devices and sophisticated image editing software allow the production of image forgeries that are virtually indistinguishable from authentic photographs. Scholars in digital image forensics aim at restoring some of the lost trustworthiness to digital images by providing tools to unveil conspicuous traces of previous image manipulations. The key point of all image forensic methods is the absence

of any prior knowledge of the original image. This obviously proves to be beneficial in many practical applications where the original data is not directly accessible.

Amongst others, resampling detection has become a standard tool for the forensic analysis of digital images. The creation of convincing image forgery oftentimes involves geometric transformations, which typically comprise a resampling of the original image to a new sampling grid. The detection of resampling is therefore of particular interest and several schemes have been proposed to address this question. As a common ground, all these detectors exploit periodic interpolation artifacts. While Popescu and Farid's state-of-the-art detector [9], to the best of our knowledge also the first proposed technique, identifies such traces in the residue of a local linear predictor, more recent algorithms analyze the variance of derivatives of a resampled image [2, 7, 11].

Inspired by these recent findings, in this paper, we will revisit Popescu and Farid's scheme and take a closer look at the origin of periodic artifacts in the *p-map* of a resampled image, which is the main output of the detector. A simplified model based on the variance of the prediction residue will serve as a tool to explain the actual appearance of the p-map and its spectral representation for arbitrary geometric transformations. This goes beyond the original work of Popescu and Farid, as they did not provide an explicit relation on how a particular transformation will influence the detector's output in the spatial and in the frequency domain. In addition, we will present an accelerated version of the original detector which bypasses the most computationally demanding elements in the detection process and at the same time provides equally reliable detection of resampling.

The rest of this paper is organized as follows. Section 2 reviews the basic principles of resampling and the detection algorithm as proposed by Popescu and Farid. In Sect. 3 we will model periodic artifacts in the p-map of a resampled signal based on the variance of the residue of the employed linear predictor and highlight implications on the detection process. Before presenting our modified detector in Sect. 5, Section 4 addresses the localization of characteristic peaks in a p-map's spectral representation. Section 6 finally reports first experimental results before Sect. 7 concludes the paper and discusses implications on related fields.

2. DETECTION OF RESAMPLING

2.1 Resampling

Oftentimes, the creation of convincing image forgery involves scaling or rotation operations. In general, such ge-

ometric transformations imply a resampling of the original image [13], i.e., a mapping of discrete integer source coordinates $\boldsymbol{\chi} = (\chi_1, \chi_2)$ to real-valued target coordinates $\boldsymbol{x} = (x_1, x_2) = \Psi(\boldsymbol{\chi})$ according to a specified mapping function $\Psi : \mathbb{Z}^2 \to \mathbb{R}^2$. In the course of this paper we will restrict ourselves to the important class of affine transformations,

$$\boldsymbol{x} = \mathbf{A}\boldsymbol{\chi} \, , \qquad (1)$$

where $\mathbf{A}$ is the 2×2 transformation matrix. Interpolation is the key to smooth and visually appealing image transformation and can be written as

$$s(\mathbf{A}\boldsymbol{\chi}') = \sum_{\boldsymbol{\chi} \in \mathbb{Z}^2} s(\boldsymbol{\chi}) h(\mathbf{A}\boldsymbol{\chi}' - \boldsymbol{\chi}) \, , \qquad (2)$$

where s is the signal of interest and $h : \mathbb{R}^2 \to \mathbb{R}^2$ is the interpolation kernel. Note that for notational convenience and without loss of generality we will focus our analysis on one-dimensional (1D) signals. Extensions to two-dimensional (2D) signals will be provided when necessary and/or useful. In the 1D case, resampling can be seen as a mapping between discrete source coordinates $\chi \in \mathbb{Z}$ and target coordinates $\omega\chi \in \mathbb{R}$, where $\omega > 0$ is the inverse resampling rate. Equation (2) reduces to

$$s(\omega\chi') = \sum_{\chi=-\infty}^{\infty} h(\omega\chi' - \chi)s(\chi) \, , \qquad (3)$$

with $\omega < 1$ for upsampling and $\omega > 1$ for downsampling.

2.2 Detection of Resampling

A virtually unavoidable side effect of typical interpolation algorithms is that they create linear dependencies between groups of neighboring samples. As shown by Gallagher [2] and Mahdian and Saic [7], the strength of dependence varies periodically with the cycle length, which itself depends on the resampling rate ω^{-1}. To the best of our knowledge, all resampling detectors exploit these periodic artifacts, which can be found in the residuals of a local linear predictor [9] as well as in the derivatives of a resampled signal [2, 7, 11].

Popescu and Farid's detector [9], probably the most extensively tested[1] and most widely used method for resampling detection, employs a linear predictor to approximate each sample's value as the weighted sum of its $2K$ surrounding samples,

$$s(\omega\chi') = \sum_{k=-K}^{K} \alpha_k s(\omega\chi' + \omega k) + e(\omega\chi') \quad \text{with } \alpha_0 := 0 \, . \quad (4)$$

A so-called p-map as a measure for the strength of linear dependence is derived from the prediction error e, which is modeled as a zero mean Gaussian random variable. Large prediction errors indicate a minor degree of linear dependence and therefore result in small values in the p-map. The core of the detection procedure is a weighted least squares (WLS) estimation of the initially unknown scalar weights $\boldsymbol{\alpha}$, incorporated into an iterative expectation maximization (EM) framework [1]. A stylized block diagram of the detection process is given in Fig. 1.

Previous resampling operations leave conspicuous pattern in the estimated p-map. The pattern becomes most evident after a transformation into the frequency domain, using a

---

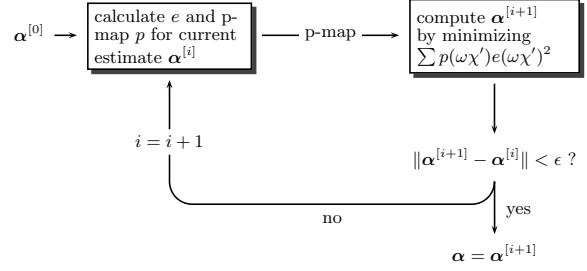[1]Test results for a wide variety of resampling parameters can be found in [8].

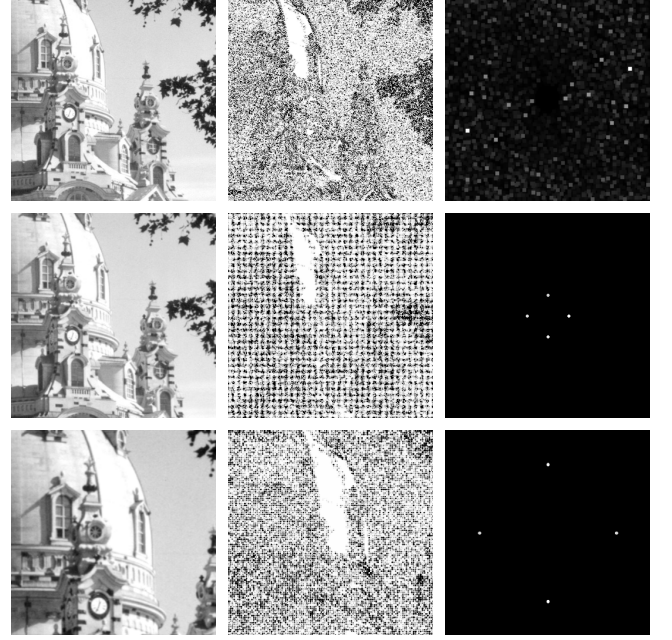**Figure 1: Iterative EM estimation of the prediction weights $\boldsymbol{\alpha}$.**

Figure 2: Results of resampling detection for original image (top row) as well as 111 % and 150 % upsampling (bottom rows). p-Maps are displayed in the middle column. Periodic resampling artefacts lead to characteristic peaks in the corresponding spectrum (rightmost pictures).

discrete Fourier transform (DFT), where it shows up as distinct peaks that are characteristic for the resampling parameters. The decision whether an image was resampled or not is made on the basis of this spectral representation, as the magnitude of distinct peaks can be easily measured in an automated process.

Figure 2 presents some typical detection results for a grey scale image which has been scaled up to 111 % ($\omega = 0.9$) and 150 % ($\omega = {}^2/_3$) of the original (left column). The calculated p-maps are displayed in the middle column. Note that only resampling causes strong periodic artifacts in the p-maps, resulting in very pronounced peaks in the spectrum.

3. ORIGIN OF PERIODIC ARTIFACTS

Although the above described detection method is already known as an effective and powerful tool, we believe that an in-depth analysis of the origin of the periodic artifacts in a

resampled image's p-map can help to further clarify *why* the rather complex detector works as it does.

Independent of Popescu and Farid's work, Gallagher [2] noticed that the variance of the second order derivative of an interpolated i.i.d. Gaussian signal is periodic with the sampling rate of the original signal. Only recently, Mahdian and Saic [7] gave an extended view and analytically showed that, under a stationary signal model, the variance of the n-th order derivative of a resampled signal is periodic with the original sampling rate.

3.1   Periodic Artifacts of the Prediction Error

To get a better understanding of the actual output of Popescu and Farid's detector, we show the relation between this method and the derivative-based approaches [2, 7] and take a closer look at the prediction error, which is obviously the origin of periodic artifacts in the p-map of a resampled signal. From Eq. (4), the residuum can be written as

$$e(\omega\chi') = s(\omega\chi') - \sum_{k=-K}^{K} \alpha_k s(\omega\chi' + \omega k) . \qquad (5)$$

Obviously, $e(\omega\chi')$ can be expressed solely in terms of original samples $s(\chi)$ by incorporating Eq. (3) as follows:

$$e(\omega\chi') = \sum_{\chi=-\infty}^{\infty} h(\omega\chi' - \chi)s(\chi)$$
$$- \sum_{k=-K}^{K} \alpha_k \sum_{\chi=-\infty}^{\infty} h(\omega\chi' + \omega k - \chi)s(\chi) \qquad (6)$$

Alternatively, we can write $e(\omega\chi')$ as a weighted sum of the actual sample of interest, $s(\omega\chi')$, and its surrounding $2K$ neighbors,

$$e(\omega\chi') = \sum_{k=-K}^{K} \beta_k \sum_{\chi=-\infty}^{\infty} h(\omega\chi' + \omega k - \chi)s(\chi) , \qquad (7)$$

with weights $\boldsymbol{\beta}$ defined as

$$\beta_k = \begin{cases} 1 & \text{for } k = 0 \\ -\alpha_k & \text{else.} \end{cases} \qquad (8)$$

Finally, by interchanging the order of summation, the residuum becomes

$$e(\omega\chi') = \sum_{\chi=-\infty}^{\infty} \varphi_\omega(\omega\chi' - \chi)s(\chi) , \qquad (9)$$

where function φ_ω is defined as

$$\varphi_\omega(x) = \sum_{k=-K}^{K} \beta_k h(x + \omega k) . \qquad (10)$$

Equation (9) reveals that $e(x)$ is basically a linearly filtered version of the original signal $s(\chi)$ with filter coefficients φ_ω derived from weighted interpolation coefficients. Note that Eq. (9) is a generalization of Gallagher's work [2], who gave an equivalent formula for a linear derivative filter.

From Eq. (9), we can compute the prediction error's variance $\text{Var}[e(x)]$ as

$$\text{Var}[e(x)] = \sum_{\chi=-\infty}^{\infty} \left[\varphi_\omega(x - \chi) \right]^2 \text{Var}[s(\chi)] +$$
$$+ 2 \sum_{\chi_1=-\infty}^{\infty} \sum_{\chi_2=\chi_1+1}^{\infty} \varphi_\omega(x - \chi_1)\varphi_\omega(x - \chi_2) \text{Cov}[s(\chi_1), s(\chi_2)] \qquad (11)$$

For our theoretical analysis we will assume $s(\chi)$ to be a wide sense stationary signal[2] with $\text{Var}[s(\chi)] = const$ and $\text{Cov}[s(\chi_1), s(\chi_2)] = \text{Cov}[s(\chi_1 + \kappa), s(\chi_2 + \kappa)]$.

THEOREM 1. *For wide sense stationary signals $s(\chi)$ with $\chi \in \mathbb{Z}$ and $\text{Var}[s(\chi)] > 0$ it holds for arbitrary prediction weights $\boldsymbol{\alpha} \neq \mathbf{0}$ and $\forall x \in \mathbb{R}$ that $\text{Var}[e(x)] = \text{Var}[e(x+1)]$.*

PROOF. Let $\Delta(x) : \mathbb{R} \to [0, 1)$ be a function defined as

$$\Delta(x) = x - \lfloor x \rfloor \qquad (12)$$

so that $\Delta(x) = \Delta(x + 1)$. We write $\text{Var}[e(x)]$ as

$$\text{Var}[e(x)] = \sum_{\chi=-\infty}^{\infty} \varphi_\omega^2(\Delta(x) - \chi) \text{Var}[s(\chi + \lfloor x \rfloor)] +$$
$$+ 2 \sum_{\chi_1=-\infty}^{\infty} \sum_{\chi_2=\chi_1+1}^{\infty} \varphi_\omega(\Delta(x) - \chi_1)\varphi_\omega(\Delta(x) - \chi_2)$$
$$\text{Cov}[s(\chi_1 + \lfloor x \rfloor), s(\chi_2 + \lfloor x \rfloor)] \qquad (13)$$

where $\varphi_\omega(\Delta(x) - \chi) = \varphi_\omega(\Delta(x+1) - \chi)$. From $\text{Var}[s(\chi)] = const$ as well as $\text{Cov}[s(\chi_1 + \lfloor x \rfloor), s(\chi_2 + \lfloor x \rfloor)] = \text{Cov}[s(\chi_1 + \lfloor x+1 \rfloor), s(\chi_2 + \lfloor x+1 \rfloor)]$ (stationarity assumption) it follows that $\text{Var}[e(x)] = \text{Var}[e(x+1)]$.   □

Basically, Theorem 1 states that for resampled stationary and non-constant signals $s(\chi)$, $\chi \in \mathbb{Z}$, the variance of a linear predictor's residuum varies with a period of 1, independent of the actual prediction weights. This specific periodicity can be inferred from the convolutive nature of kernel-based interpolation, which employs the very same interpolation weights to determine new samples at positions x and $x + 1$. With 1 being the original sampling rate, Theorem 1 shows a relation between the derivative-based detection schemes and Popescu and Farid's detector.

It is straightforward to show that Theorem 1 also holds for two-dimensional resampled stationary signals. In this case, $\text{Var}[e(x_1, x_2)]$ is periodic in both dimensions, thus

$$\text{Var}[e(x_1, x_2)] = \text{Var}[e(x_1 + 1, x_2)] =$$
$$\text{Var}[e(x_1, x_2 + 1)] = \text{Var}[e(x_1 + 1, x_2 + 1)] . \qquad (14)$$

3.2   Why Periodic Variance Matters

As described in Sect. 2.2, Popescu and Farid's detector [9] models $e(\omega\chi')$ as a $\mathcal{N}(0, \sigma)$ Gaussian random variable. According to the employed model, larger prediction errors correspond to less linear dependence and thus yield smaller values in the p-map. From Theorem 1 we can infer that the theoretically derived variance of the prediction error periodically varies throughout the whole signal. Since a large

---

[2]This is a reasonable assumption especially for homogeneous parts of a signal.
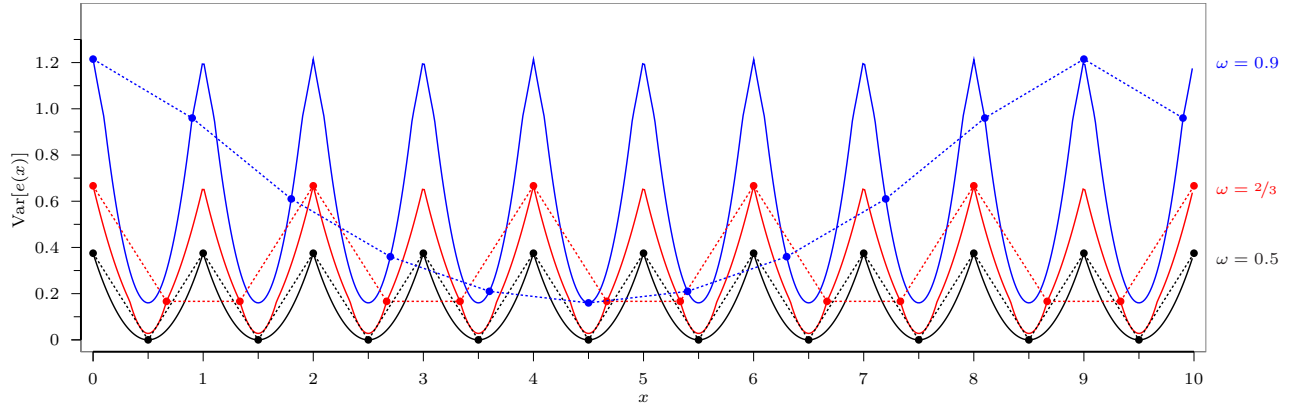
13

Figure 3: Periodic artifacts in the variance of the prediction error. Theoretical graphs (solid lines) for sample resampling rates together with their sampled versions (dashed lines). Inverse resampling rates $\omega > 0.5$ will cause aliasing frequencies.

variance increases the probability of a large prediction error and vice versa, the identified periodicity of variance can serve as a simplified model to explain the observed periodic artifacts in the p-map of a resampled signal.

3.3 Periodic Artifacts in Resampled Signals

To reveal the relation between the theoretical periodicity and the actually observed pattern in a p-map, we note that in resampled signals $s(\omega\chi)$, $\mathrm{Var}[e(x)]$ is sampled with a frequency $f_s = \omega^{-1}$, Eq. (11). As $\mathrm{Var}[e(x)]$ is periodic with 1, the Nyquist criterion states that the original periodicity is only preserved for $f_s \geq 2$. Figure 3 shows the continuous (theoretical) graphs of $\mathrm{Var}[e(x)]$ for exemplary resampling rates (solid lines) together with their sampled versions $\mathrm{Var}[e(\omega\chi)]$ (dashed lines) for an i.id. Gaussian signal with $\mathrm{Var}[s(\chi)] = 1$. The weights have been chosen as $\boldsymbol{\beta} = (-0.5, 1, -0.5)$. Observe that in our example both $\omega = {}^2\!/_3$ and $\omega = 0.9$ do not fulfill the Nyquist criterion and thus result in an increased period. The depicted graphs conform to Fig. 2, where resampling with $\omega = 0.9$ yields a p-map with a much larger period than resampling with $\omega = {}^2\!/_3$.

It is interesting to mention that the chosen weights are closely connected to the second order derivative, typically calculated as $2s(\omega\chi) - s(\omega\chi - \omega) - s(\omega\chi + \omega)$. This reveals a strong parallel between Popescu and Farid's detector and the resampling detectors based on the variance of the signal's derivatives [2, 7].

Note that for 2D signals, $\mathrm{Var}[e(x_1, x_2)] = \mathrm{Var}[e(\mathbf{x})]$ is sampled in two dimensions. For an affine transformed signal, sampling of $\mathrm{Var}[e(\mathbf{x})]$ can be understood as sampling of an accordingly transformed version $\mathrm{Var}[e(\tilde{\mathbf{x}})] = \mathrm{Var}[e(\mathbf{A}\mathbf{x})]$, where $\mathbf{A}$ is the 2×2 affine transformation matrix and the sampling frequencies are given by $\mathbf{f}_s = (1, 1)$.

3.4 Implications

In the following, we will highlight three implications which follow directly from our findings in the previous section and especially from Theorem 1.

1. Using the simplified model for periodic artifacts in the p-map of a resampled signal, we can employ basic signal processing primitives to derive an exact formula-

tion on how a specific transformation will influence the position of the characteristic peaks in the p-map's spectrum.

2. Furthermore, and probably most important, the detector's prediction error will exhibit periodic traces of resampling independent of the actual prediction weights. We therefore believe that a rather complex and time-consuming EM estimation of $\boldsymbol{\alpha}$ is not compulsory. In the most simple case, resampling detection involves only linear filtering with preset filter coefficients.

3. For the same reason, the size of the prediction neighborhood K is only of minor influence.

All these issues will be analyzed in more detail in the following sections. More specifically, Sect. 4 will present formulas to predict the expected location of characteristic peaks in a p-map's spectrum by adopting basic principles from sampling theory. Afterwards, based on implication 2, we will propose a fast and simplified detector with comparable reliability, which will be evaluated experimentally in Sect. 6, together with a study on the influence of different prediction neighborhoods.

4. LOCATING CHARACTERISTIC PEAKS

Section 3 highlighted that the formation of periodic artifacts in the p-map of a resampled signal can be idealized as sampling of the periodic variance of the detector's prediction error. Below, we will use this model to analytically derive the characteristic peaks in a p-map's spectral representation.

4.1 1D Signals

Let V be the Fourier transformation of $\mathrm{Var}[e(x)]$, i.e., $V = \mathcal{F}(\mathrm{Var}[e(x)])$. As $\mathrm{Var}[e(x)]$ is periodic with 1, V has a distinct peak at $|f_p| = 1$.

It is well known from signal processing theory that the Fourier transformation of a sampled signal is a periodic extension of the original spectrum, where the period is given by the sampling frequency f_s. Let V_ω be the discrete Fourier transformation (DFT) of $\mathrm{Var}[e(\omega\chi)]$,

$$V_\omega = \sum_{n=-\infty}^{\infty} V(f - nf_s) = \sum_{n=-\infty}^{\infty} V\left(f - n\omega^{-1}\right). \quad (15)$$
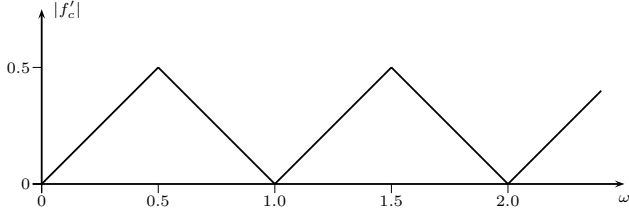
Figure 4: Normalized characteristic peak position $|f'_c|$ for 1D resampling. Different inverse resampling rates ω result in the same peak position.

The baseband of V_ω is given by $-1/2\omega \leq f \leq 1/2\omega$. As was already mentioned in Sect. 3.3, "correct" sampling implies $f_p \leq 1/2\omega$ and thus $\omega \leq 0.5$. In this case, the characteristic peaks in the p-map's spectrum are directly given by ± 1. Otherwise aliasing occurs, which means that so called <mark>alias frequencies</mark> from high frequency bands will appear as characteristic peaks in the baseband.

Let $f' = f\omega$ be a normalized frequency with a normalized baseband $-0.5 \leq f' \leq 0.5$. The characteristic peaks $\pm f'_c$ in a p-map's baseband spectral representation are then given by

$$|f'_c| = 0.5 - |\Delta(\omega) - 0.5|$$
$$= \begin{cases} \Delta(\omega) & \text{for } \Delta(\omega) \leq 0.5 \\ 1 - \Delta(\omega) & \text{for } \Delta(\omega) > 0.5 \end{cases} \quad (16)$$

This can be shown by noting that $f_p = 1$ will yield distinct peaks at normalized alias frequencies $\omega - n, n \in \mathbb{Z}$. If we write ω as $\omega = m + y, m \in \mathbb{N}, y \leq 1$, then $y = \Delta(\omega)$ is an alias of f_p as well. Obviously, Eq. (16) gives the correct baseband alias of $f_p = 1$ for $\Delta(\omega) \leq 0.5$. For $\Delta(\omega) > 0.5$, the baseband alias is given by $\Delta(\omega) - 1$, which complies with Eq. (16) as well.

Apparently, Eq. (16) can be used to reason about the expected characteristic peak position in a p-map's spectral representation for a given ω. However, it should be noted that an unique inverse mapping is not possible. To demonstrate the ambiguity in the formation of the characteristic peaks, Fig. 4 shows a plot of $|f'_c|$ as a function of ω. Obviously, two resampling rates ω_1 and ω_2 will produce the same peaks, if $\omega_1 = n + \omega_2$ or $\omega_1 = n + 1 - \omega_2, \forall n \in \mathbb{N}$.

4.2 2D Signals

In order to adapt the insights of the previous section to two-dimensional signals, we note that due to Eq. (14) $V = \mathcal{F}(\text{Var}[e(\mathbf{x})])$ has distinct peaks at $\mathbf{f}_{p_1} = (1,0)$, $\mathbf{f}_{p_2} = (0,1)$ and $\mathbf{f}_{p_3} = (1,1)$ (and the corresponding peaks due to symmetry of the spectrum). From [4, p. 53]

$$\mathcal{F}(\text{Var}[e(\mathbf{A}\mathbf{x})]) = \frac{1}{\det \mathbf{A}} V\left((\mathbf{A}')^{-1}\mathbf{f}\right) \quad (17)$$

follows that the spectrum of the variance of an affine transformed version e exhibits distinct peaks at $(\mathbf{A}')^{-1}\mathbf{f}_{p_i}, i = 1, 2, 3$. As with the 1D case, sampling implies a periodic extension of the original spectrum (this time in two dimensions),

$$V_\mathbf{A} = \sum_{\forall \mathbf{n} \in \mathbb{Z}^2} V\left((\mathbf{A}')^{-1}\mathbf{f} - \mathbf{n}\right) . \quad (18)$$
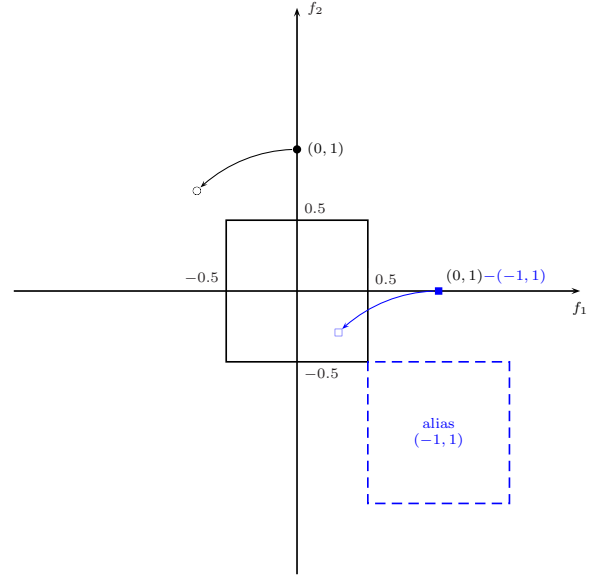

Figure 5: Characteristic peaks as a result of aliasing for 2D resampling (counterclockwise rotation of $45°$). Characteristic peak in the baseband (solid square) originates from high frequency alias $(-1, 1)$.

Note, that we have dropped the scalar term from Eq. (17) as we are mainly interested in the peak position. The baseband of $V_\mathbf{A}$ is given by $(|f_1|, |f_2|) = |\mathbf{f}| \leq (0.5, 0.5)$, thus aliasing-free sampling requires $|(\mathbf{A}')^{-1}\mathbf{f}_{p_i}| \leq (0.5, 0.5)$. Otherwise, alias frequencies from high frequency bands will appear as characteristic peaks in the baseband.

Figure 5 demonstrates the formation of characteristic baseband peaks from high frequency aliases for a $45°$ counterclockwise rotation. The filled dot in the two-dimensional frequency plane marks the original peak $\mathbf{f}_{p_2} = (0,1)$. Due to rotation, the peak is transformed to $(\mathbf{A}')^{-1}\mathbf{f}_{p_2}$. Since, for plain rotation, $(\mathbf{A}')^{-1} = \mathbf{A}$, the transformation solely comprises a rotation of the original peak (plain circle). The baseband is given by $|\mathbf{f}| \leq (0.5, 0.5)$ and therefore $(\mathbf{A}')^{-1}\mathbf{f}_{p_2} = (-\sin \pi/4, \cos \pi/4)$ is located outside the baseband. Nevertheless, an alias of $\mathbf{f}_{p_2}$ will appear in the baseband (plain square), namely those for $\mathbf{n} = (-1, 1)$.

The calculation of the normalized characteristic baseband peaks $\mathbf{f}'_{c_i}$ for a given transformation $\mathbf{A}$ follows straightforward from the one-dimensional case. According to Eq. (18) the baseband of $V_\mathbf{A}$ is already equivalent to a normalized baseband with $|\mathbf{f}'| \leq (0.5, 0.5)$. In order to use a consistent notation, we will therefore simply write $\mathbf{f}' = \mathbf{f}$. The three distinct original peaks $\mathbf{f}_{p_i}$ will yield normalized peaks at $\mathbf{f}'_{p_i} - \mathbf{n}, \mathbf{n} \in \mathbb{Z}^2$, where

$$\mathbf{f}'_{p_i} = (\mathbf{A}')^{-1}\mathbf{f}_{p_i} . \quad (19)$$

Adapting Eq. (16) to the two-dimensional case, the baseband characteristic peaks can be calculated as

$$|\mathbf{f}'_{c_i}| = \mathbf{b}' - |\Delta(\mathbf{f}'_{p_i}) - \mathbf{b}'| , \quad (20)$$

with $\mathbf{b}' = (0.5, 0.5)$ denoting the normalized baseband and $\Delta(\mathbf{f}) = (\Delta(f_1), \Delta(f_2))$.

Figure 6 gives a concluding example for the location of characteristic resampling peaks by depicting p-maps and
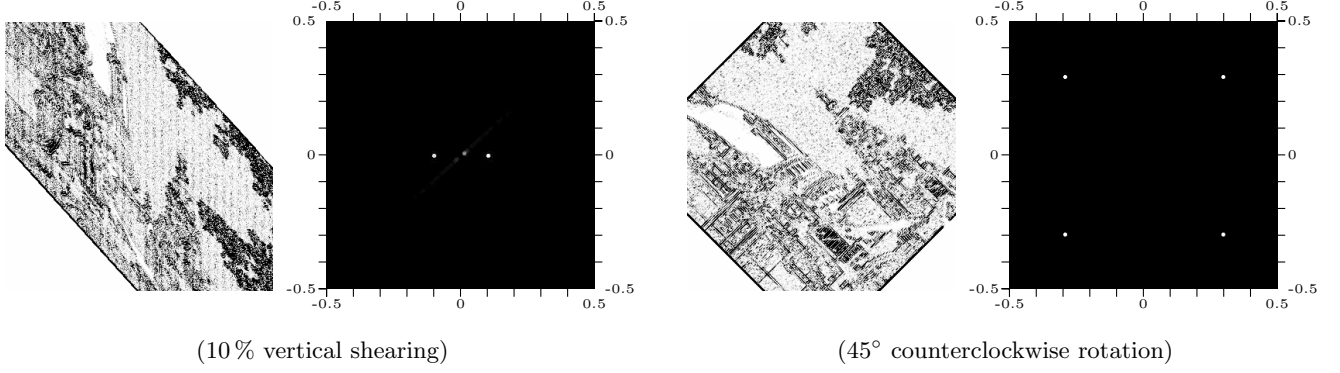
(10 % vertical shearing)   (45° counterclockwise rotation)

Figure 6: p-maps and peak position in 2D for sample shearing (left) and rotation (right) transformations.

their spectra for shearing (left) and counterclockwise rotation (right), respectively. More specifically, transformation matrices

$$\mathbf{A}_1 = \begin{bmatrix} 1 & 0 \\ 1.1 & 1 \end{bmatrix} \quad \text{and} \quad \mathbf{A}_2 = \begin{bmatrix} \cos \pi/4 & \sin \pi/4 \\ -\sin \pi/4 & \cos \pi/4 \end{bmatrix}$$

have been used to achieve 10 % vertical shearing and 45° rotation of the test image from Fig. 2. From Eq. (20), we expect shearing peaks at $\mathbf{f}'_{c_1} = (0, 0)$ and $\mathbf{f}'_{c_2} = \mathbf{f}'_{c_3} = (0.1, 0)$ as well as rotation peaks at $\mathbf{f}'_{c_1} = \mathbf{f}'_{c_2} = (0.293, 0.293)$ and $\mathbf{f}'_{c_3} = (0.414, 0)$. Observe that the determined peaks in Fig. 6 concur with the theoretically calculated peak positions. It is worth mentioning that a peak at (0,0) interferes with the DC component and is therefore not detectable.[3] Furthermore, we found that $\mathbf{f}_{c_3}$ (the one originating from diagonal periodicity) is typically less prominent.

5. FAST DETECTION OF RESAMPLING

In the remainder of this paper we will present an accelerated version of Popescu and Farid's resampling detector which is orders of magnitudes faster than the original algorithm and at the same time provides comparable accuracy. Basically, our modifications are twofold as we will

1. replace the complex and time-consuming EM estimation of the scalar weights $\boldsymbol{\alpha}$ with fast linear filtering with preset coefficients, and

2. propose a fast procedure to automatically detect the presence of characteristic peaks in a p-map's spectrum.

While the first modification directly follows from Sect. 3.4, the second variation will be shown to be a simplified heuristic for an automated analysis of resampling artifacts.

5.1 Fast Computation of the p-Map

Remember that the original detection scheme involved an iterative execution of a weighted least squares (WLS) estimator in order to obtain a stable estimate of the prediction weights $\boldsymbol{\alpha}$. Section 3 suggests that the prediction error of resampled signals will exhibit periodic artifacts independent of the actual weights. Our modified detector will thus bypass the computationally demanding EM estimation of the scalar weights by using a linear filter with preset coefficients,

---

[3]The DC component is missing as we computed the DFT from <mark>zero mean p-maps.</mark>

which will result in a tremendous speed up of the detector, cf. Tab. 1 in the Appendix.

Once the prediction error e has been determined, cf. Eq. (5), we determine the p-map similar to Popescu and Farid's Gaussian distribution based calculation as

$$p = \lambda \exp\left(-\frac{|e|^\tau}{\sigma}\right) , \qquad (21)$$

where $\lambda, \sigma > 0$ and $\tau \geq 1$ are controlling parameters. Basically, p can be seen as a <mark>contrast function,</mark> which penalizes larger absolute values of e with smaller resulting values in the corresponding p-map.

5.2 Automatic Detection of Resampling

Although a human investigator might be well able to identify periodic traces of resampling in the p-map of a given signal, a detector which can reliably distinguish between original and resampled signals in an automated batch process is highly desirable.

5.2.1 Automatic Detection via Exhaustive Search

In order to automatically decide whether an signal was resampled or not, Popescu and Farid [9] propose to transform the signal's p-map to the frequency domain using the discrete Fourier transform (DFT). Periodic pattern in the p-map will yield distinct peaks in the spectral representation, cf. Sect. 4. Strength and visibility of the characteristic peaks are enhanced by using a <mark>contrast function.</mark> The function is composed of a <u>radial weighting window</u>, which attenuates low frequency noise, and a <u>gamma correction step</u>. The detector's final decision is based on the similarity between the p-map of the given signal and elements of a candidate set of synthetically generated periodic patterns. Popescu and Farid [9] gave an empirically derived formula, how to calculate a synthetic map $\rho^{(\mathbf{A})}$ for an affine transformation matrix $\mathbf{A}$. As the detector lacks any prior knowledge about the actual transformation parameters, the detection process involves an exhaustive search in a sufficiently large set $\mathcal{A}$ of candidate transformation matrices. The maximum pairwise similarity between an empirical p-map and all elements of $\mathcal{A}$ is taken as a decision criterion δ,

$$\delta = \max_{\mathbf{A} \in \mathcal{A}} \sum_{|\mathbf{f}| \leq \mathbf{b}} \left| \Gamma(\mathrm{DFT}(p)) \right| \odot \left| \mathrm{DFT}\left(\rho^{(\mathbf{A})}\right) \right|, \qquad (22)$$

where <mark>Γ is the contrast function.</mark> If δ exceeds a specific

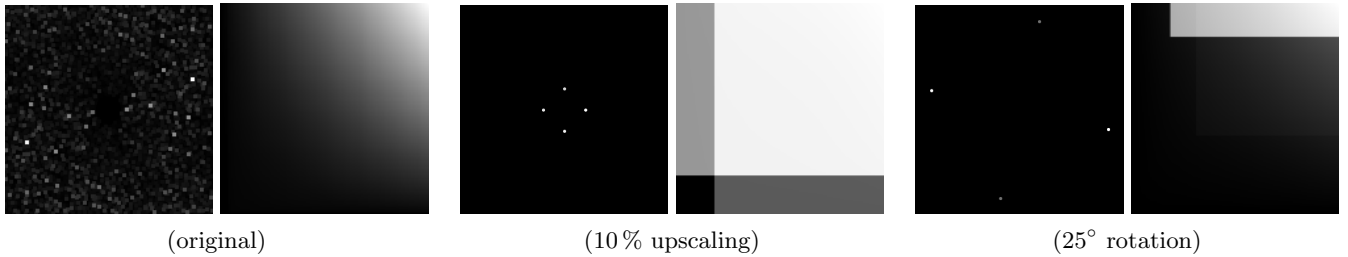|		
(original)	(10 % upscaling)	(25° rotation)

Figure 7: Spectra and cumulative periodograms of p-maps for original, 10 % upscaled and 25° rotated test image (from left to right). In each case, the baseband spectrum is shown on the left and the cumulative periodogram of the first quadrant is shown on the right. Resampling yields sharp-edged periodograms.

threshold δ_T, the corresponding signal is flagged as resampled.

One of the drawbacks of the procedure is that approximate synthetic maps ρ are needed, which happen to be noisy and error-prone. More specifically, we found that some synthetic maps exhibit relatively strong secondary frequency components other than the one originally intended. However, we want to point out that this is not a serious problem in laboratory tests, as all reported results in the literature attest a very high detection accuracy [6, 8, 9]. Nevertheless, from Sect. 4, we know that we could do even better by generating *exact* synthetic spectra for a given matrix **A**.

5.2.2 Automatic Detection with Cumulative Periodograms

A much larger drawback lies in Eq. (22) itself, as the detector has to perform an exhaustive search over all candidate matrices in order to decide whether the signal of interest has been resampled or not. Obviously, the set $\mathcal{A}$ will become very large in practical scenarios where the detector has to cover a wide variety of possible transformations. Ultimately, we can never be sure whether the signal has not been manipulated or whether the detector has just failed because of missing the correct transformation matrix.

As one possible way out, we will employ the *cumulative periodogram*, which is used in time series analysis to detect the presence of particular frequency components. A 2D version can be calculated from the first quadrant of a p-map's DFT ($0 \leq \mathbf{f} \leq \mathbf{b}$) as

$$C(\mathbf{f}) = \sum_{0 < \mathbf{f}' \leq \mathbf{f}} |P(\mathbf{f}')|^2 \cdot \left(\sum_{0 < \mathbf{f}' \leq \mathbf{b}} |P(\mathbf{f}')|^2 \right)^{-1} , \qquad (23)$$

where P denotes $\Gamma(\mathrm{DFT}(p))$ and $C \in [0, 1]$.

Figure 7 depicts spectrum and cumulative periodogram of the p-maps of our original test image, a 10 % upscaled version as well as a 25° rotated version (from left to right). Observe that while the original cumulative periodogram is well characterized by a smooth gradient from low (bottom left) to high (top right) frequencies, the periodograms of the processed versions exhibit sharp transitions due to the existence of distinct peaks in the spectrum.

As distinct peaks from periodic artifacts will cause a sharp-edged cumulative periodogram we take the maximum absolute gradient of the cumulative periodogram as a new decision criterion δ',

$$\delta' = \max_{\mathbf{f}} |\nabla C(\mathbf{f})| , \qquad (24)$$

where ∇ is the gradient operator. If δ' exceeds a specific threshold δ'_T, the corresponding signal is flagged as resampled. Note that the computation of the new decision criterion does not involve an exhaustive search in a set of possible candidate transformations. Instead, we base our decision solely on the discriminative feature of prominent gradients in the cumulative periodogram of a resampled signal's p-map, which can be directly derived from the signal itself. An automatic detection via cumulative periodograms is therefore much less computationally demanding and at the same time not blind to "unknown" transformation parameters.

6. EXPERIMENTAL RESULTS

For an experimental evaluation of our modified detector we use a database of 200 never-compressed 8 bit grayscale images. All images were taken with a Canon PowerShot S70 digital camera at full resolution (3112×2382 pixels). In order to preclude possible interferences from periodic patterns which might stem from a color filter array (CFA) interpolation inside the camera [10], each image was downsampled by factor two using nearest neighbor interpolation. Detection results are given for a subset of 100 randomly chosen images, each resized and rotated by various degrees using linear interpolation. The performed transformations are parametrized by inverse scaling rates $\omega^{-1}, 0.5 \leq \omega^{-1} \leq 2$ and counterclockwise rotation angles $\Theta, 0 < \Theta \leq 45$, respectively. To limit the computation time of the original detection scheme, the transformed images were cropped to 256×256 pixels prior to analysis.

When employing the original detector, a set of altogether 692 synthetic maps is used to compute the decision criterion δ, cf. Eq. (22). More specifically, we use 601 maps for scaling in the range of $0.5 \leq \omega^{-1} \leq 2$, with ω^{-1} sampled in steps of $\Delta\omega^{-1} = 0.0025$ and 91 maps for rotation in the range of $0 \leq \Theta \leq 45$, with Θ sampled in steps of $\Delta\Theta = 0.5$.

The detection thresholds δ_T and δ'_T have been determined empirically for defined false acceptance rates (FAR) by applying the detectors to all 200 images in the database.

6.1 Size of Prediction Neighborhood

In their original paper [9], Popescu and Farid use a 5×5 ($K = 2$) prediction neighborhood in order to detect traces of resampling in digital images. As they did not provide a strong motivation for this particular choice, we are interested in how the size of the prediction neighborhood influences the detection accuracy.

Remember that in Sect. 3.4, we argued that due to Theorem 1 the size of the comprised neighborhood has only minor
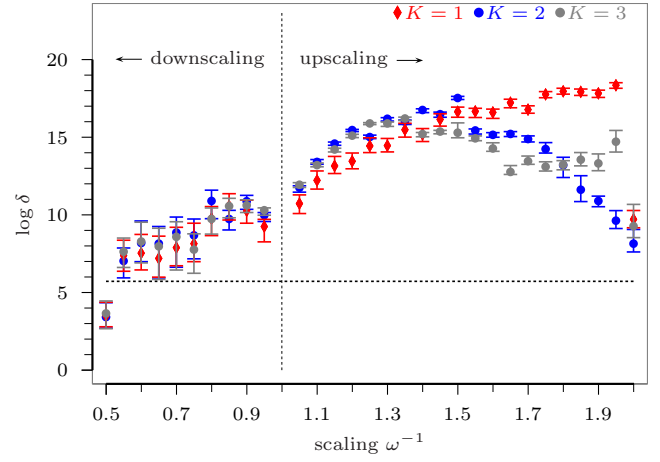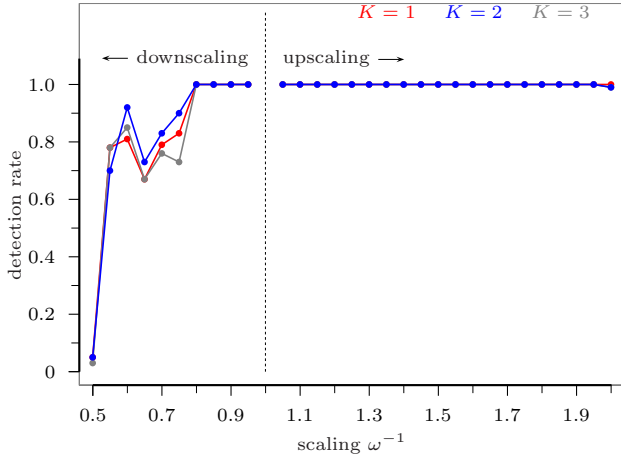
Figure 8: Detection rates (left) and decision criterion (right) for the original detector and varying prediction neighborhood sizes and scaling factors (FAR $\leq 1\,\%$). Right: Solid dots denote median values, $25\,\%$ and $75\,\%$ quantiles are represented by attached lower and upper bars.

impact on the detector's output. Figure 8 depicts detection results of Popescu and Farid's detector for scaling and prediction neighborhoods of size $3 \times 3, (K = 1)$, $5 \times 5, (K = 2)$ and $7 \times 7, (K = 3)$, respectively. More specifically, detection rates for a false acceptance rate of FAR $\leq 1\,\%$ are shown on the left and corresponding values of the decision criterion δ are reported on the right. Here, solid diamonds denote the median value of δ for a specific scaling rate, whereas the $25\,\%$ and $75\,\%$ quantiles are represented by the attached lower and upper bars. The horizontal dashed line corresponds to the $99\,\%$ quantile for the original images (FAR $\leq 1\,\%$) for a 3×3 neighborhood. As the threshold is nearly constant for all tested sizes, we refrain from plotting them all separately.

As we can see from the left graph, detection rates differ only marginally for different neighborhood sizes, which conforms to our initial conjecture. Upsampling is perfectly detected, downsampling is detectable with high accuracy (except for $\omega^{-1} = 0.5$).Nevertheless, a comparison of the corresponding decision criteria reveals that there are measurable differences especially for strong upsampling. Interestingly, $K = 1$ (3×3 neighborhood) is the best performer for $\omega^{-1} > 1.5$. However, it seems hard to gather a general rule, as $K = 2$ lies more or less in between its smaller and larger alternatives.

Overall, the observed invariance of the detection rate to different neighborhood sizes is a very interesting result, as larger prediction neighborhoods typically increase the computing time necessary to arrive at a stable estimate of the prediction weights $\boldsymbol{\alpha}$, cf. Tab. 1 in the Appendix. From our experiment we may conclude that a straightforward "speed up" of the detector thus simply suggests the use of a small 3×3 prediction mask.

6.2   Performance of the Accelerated Detector

As was described in Sect. 5.1, a much more substantial saving in computation time can be achieved by dropping the EM estimation of the prediction weights. Before presenting detection rates for the simplified detector, we will have a look at the actual estimates of the original detector. Adhering to Sect. 6.1, we will focus on 3×3 neighborhoods only.
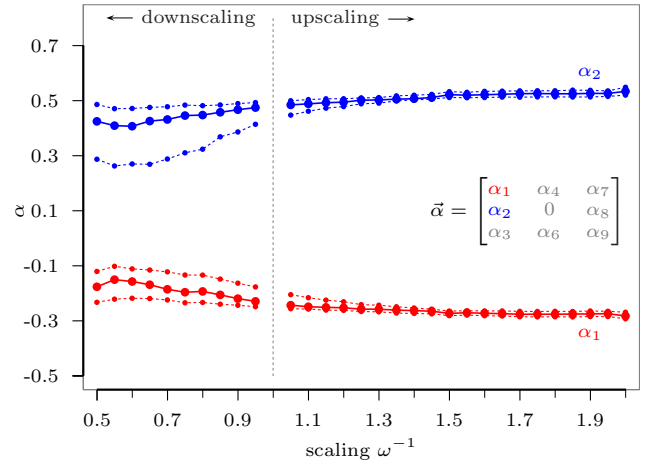

Figure 9: Scalar weights α_1 and α_2 for varying scaling factors, as estimated with the EM algorithm. Median values (solid line) together with $25\,\%$ and $75\,\%$ quantiles (dashed lines) from 100 images.

Figure 9 depicts the estimated weights for scaling of 100 images, each at varying scaling factors. The detector was initialized with $\alpha_i^{[0]} = 1/((2K + 1)^2 - 1)$. Writing $\boldsymbol{\alpha}$ as

$$\boldsymbol{\alpha} = \begin{bmatrix} \alpha_1 & \alpha_4 & \alpha_7 \\ \alpha_2 & 0 & \alpha_8 \\ \alpha_3 & \alpha_6 & \alpha_9 \end{bmatrix},$$

we found that the estimate typically shows a strong symmetry, namely $\alpha_1 \approx \alpha_3 \approx \alpha_7 \approx \alpha_9$ and $\alpha_2 \approx \alpha_4 \approx \alpha_6 \approx \alpha_8$. Figure 9 therefore contains plots for α_1 and α_2 only. Dots connected with a solid line denote median values; dashed lines below and above correspond to the $25\,\%$ and $75\,\%$ quantiles. Observe that the median estimates are on a nearly constant level throughout all scaling rates whereas upscaling estimates show virtually no considerable variation. The depicted graphs thus encourage us even more to omit the EM estimation of the prediction weights.
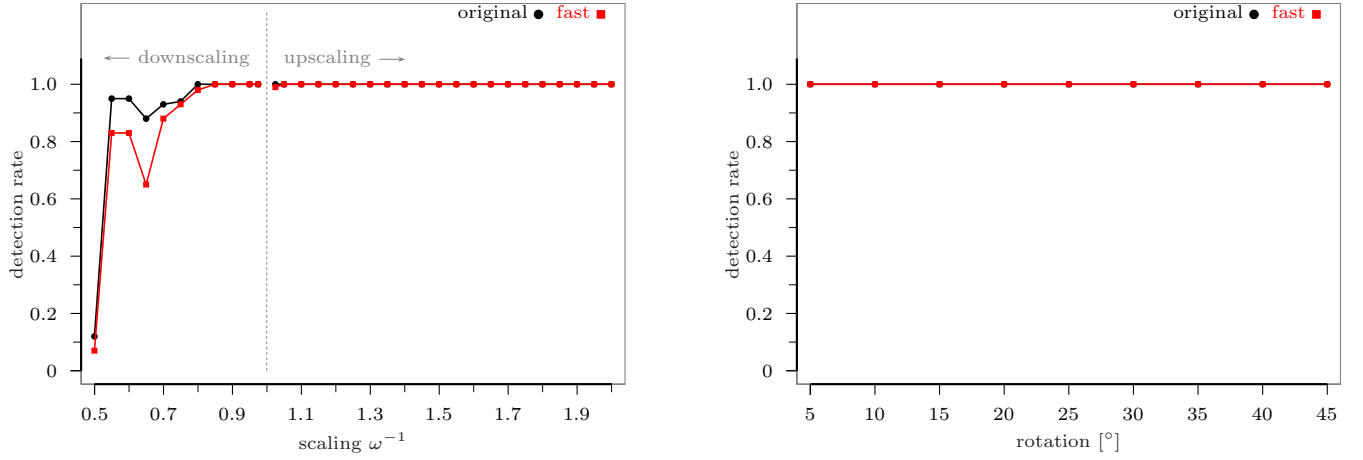
Figure 10: Detection rates at FAR ≤ 3 % of the modified fast detector together with results of the original scheme for scaling (left) and rotation (right). Perfect detection of upscaling and rotation as well as high detection accuracy for downscaling for both detectors.

Figure 9 will act as an indicator for the setup of the fast resampling detector. More specifically, we used preset filter coefficients $\boldsymbol{\alpha}^*$ for the computation of the prediction error,[4]

$$\boldsymbol{\alpha}^* = \begin{bmatrix} -0.25 & 0.50 & -0.25 \\ 0.50 & 0 & 0.50 \\ -0.25 & 0.50 & -0.25 \end{bmatrix} . \qquad (25)$$

The controlling parameters have been fixed to $\lambda = 1, \sigma = 1$ and $\tau = 2$ throughout all experiments. In order to determine the decision criterion δ', we employ a Sobel edge detector, a well-known image processing primitive which is often used as a simple approximation of the gradient operator [4].

Figure 10 depicts detection rates for scaling (left) and rotation (right) of the modified detector at a false acceptance rate of FAR ≤ 3 %. The results of the original detector are included as reference. The graphs indicate that the accelerated version performs equally well for the vast majority of the tested transformation parameters.[5] As with the original scheme, upscaling and rotation are perfectly detected. Strong downscaling is the weak point of our modified scheme, since Popescu and Farid's detector gives slightly better detectability here. For a better comparison, complete ROC curves for downscaling with $\omega^{-1} = 0.55$ and upscaling with $\omega^{-1} = 1.1$ are reported in Fig. 11. We found these transformation parameters to be good representatives to highlight the characteristics of the modified detector. As was already suggested by Fig. 10, performance under upscaling (as well as rotation) transformations is absolutely equivalent to the much slower (cf. Tab. 1 in the Appendix) original scheme. Downscaling is still well detectable, however we acknowledge that the results achieved so far leave room for further improvements. Nevertheless, we believe that the reported detection rates legitimate future research and fine-tuning. Especially the controlling parameters τ, σ

---

[4]This conforms to a recent study [5], in which the authors found empirically that for WS-like steganalysis $\boldsymbol{\alpha}^*$ is the best predictor to minimize the L^2 distance between a cover image predicted from a stego image and the true cover.

[5]Detection rates as achieved with the original decision criterion δ were found to be virtually identical and are therefore not reported here.
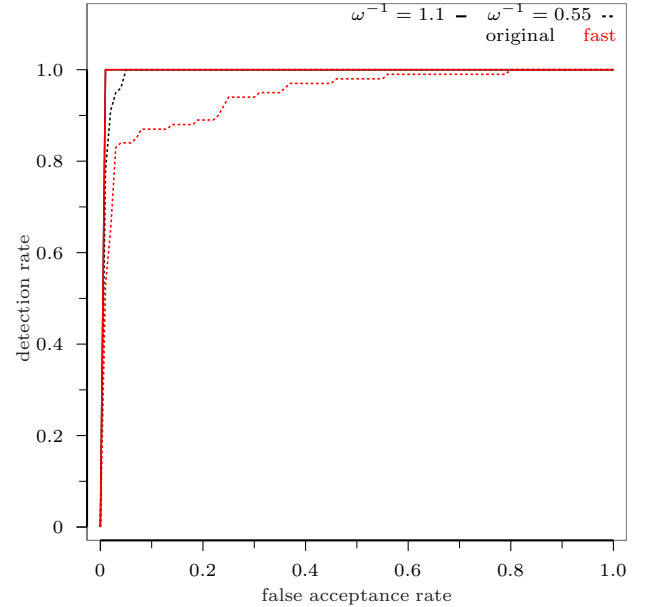

Figure 11: ROC curves of the modified detector (solid lines) together with results of the original scheme (dashed lines) for downscaling ($\omega^{-1} = 0.55$) and upscaling ($\omega^{-1} = 1.1$).

as well as the contrast function Γ are natural candidates for fine-tuning and adjusting the detector.

7. CONCLUDING REMARKS

In this paper, we have revisited the state-of-the-art resampling detector as proposed by Popescu and Farid [9]. We have taken a closer look at the origin of periodic artifacts in a resampled signal's p-map, which is the main output of the detector, and have shown relations between this scheme and more recent derivative-based approaches [2, 7]. The main contribution of this paper is twofold. First, we have presented a simple model to explain the actual shape

of periodicity which can be expected in a p-map for a specific geometric transformation. Second, we have proposed an accelerated version of the detector.

More specifically, we have shown how the variance of prediction residuals of a resampled signal can be used to describe periodic artifacts in the corresponding p-map. A calculation of the exact expected position of characteristic peaks in the p-map's spectrum for arbitrary geometric transformations of both one-dimensional and two-dimensional signals was inferred from this model.

By recognizing that the formation of periodic artifacts does not depend on the actual prediction weights, we proposed a simplified detector which replaces the complex and computationally demanding estimation of prediction weights by linear filtering with fixed filter coefficients. For an automated detection scenario, an additional performance gain was achieved by replacing the exhaustive search in a set of candidate transformations with a much faster search for anomalies in the p-maps' cumulative periodogram. Experimental results on a large image database confirm that the new detector is orders of magnitudes faster than the original scheme and at the same time comparably reliable.

Our future research will include a quantitative validation of our model of periodic artifacts with respect to the correctness of the predicted peak position in a p-map's spectrum. Some effort might be spent on resolving the identified ambiguities in the expected position of characteristic peaks by means of additional features, e.g., level the of detail in the image under investigation. A more comprehensive quantitative performance comparison will also benchmark our fast detector with Mahdian and Saic's derivative-based detector [7]. Finally, we will address the identified performance differentials in the detection of strong downscaling.

It is important to mention that – similar to the original scheme – our modified detector is expected to be vulnerable to recently presented geometric distortion attacks against resampling detection [6]. However, an analysis of the inserted distortion, in terms of sampling the periodic variance of the prediction error with randomized sampling frequencies, appears to be a promising direction in order to derive possible countermeasures.

On a more general level this paper offers some prospects for related fields. The possibility to locate characteristic resampling peaks can help to reduce the search space in the re-synchronization of geometrically transformed images, which is of particular interest in camera identification [3] and watermark detection

8. ACKNOWLEDGMENTS

9. REFERENCES

[1] A. Dempster, N. Laird, and D. Rubin. Maximum likelihood from incomplete data via the EM algorithm. *Journal of the Royal Statistical Society, Series B*, 39(1):1–38, 1977.

[2] A. C. Gallagher. Detection of linear and cubic interpolation in JPEG compressed images. In *Proceedings of the Second Canadian Conference on Computer and Robot Vision*, 65–72, 2005.

[3] M. Goljan and J. Fridrich. Camera identification from scaled and cropped images. In E. J. Delp et al., editors, *Security, Forensics, Steganography, and Watermarking of Multimedia Contents X*, volume 6819, 68190E, 2008.

[4] B. Jähne. *Digital Image Processing*. Springer-Verlag, Berlin, Heidelberg, 6th edition, 2005.

[5] A. D. Ker and R. Böhme. Revisiting weighted stego-image steganalysis. In E. J. Delp et al., editors, *Security, Forensics, Steganography, and Watermarking of Multimedia Contents X*, volume 6819, 681905, 2008.

[6] M. Kirchner and R. Böhme. Tamper hiding: Defeating image forensics. In T. Furon et al., editors, *Information Hiding, 9th International Workshop*, LNCS 4567, 326–341, Berlin, Heidelberg, 2007. Springer Verlag.

[7] B. Mahdian and S. Saic. On periodic properties of interpolation and their application to image authentication. In *Third International Symposium on Information Assurance and Security*, 439–446, 2007.

[8] A. C. Popescu. *Statistical Tools for Digital Image Forensics*. PhD thesis, Department of Computer Science, Dartmouth College, Hanover, NH, USA, 2005.

[9] A. C. Popescu and H. Farid. Exposing digital forgeries by detecting traces of re-sampling. *IEEE Trans. on Signal Processing*, 53(2):758–767, 2005.

[10] A. C. Popescu and H. Farid. Exposing digital forgeries in color filter array interpolated images. *IEEE Trans. on Signal Processing*, 53(10):3948–3959, 2005.

[11] S. Prasad and K. Ramakrishnan. On resampling detection and its application to detect image tampering. In *Proceedings of the 2006 IEEE International Conference on Multimedia and EXPO*, 1325–1328, 2006.

[12] H. T. Sencar and N. Memon. *Overview of State-of-the-art in Digital Image Forensics*. World Scientific Press, 2008.

[13] G. Wolberg. *Digital Image Warping*. IEEE Computer Society Press, Los Alamitos, CA, USA, 3. edition, 1994.

APPENDIX

Table 1 reports average computing times together with the average number of iterations for the original detector with different neighborhood sizes as well as average computing times for the modified detector. The results were obtained by running modestly optimized C implementations of both detectors on 20 grayscale images of size 512×512 on a 2.2 GHz, 2 GB memory, dual core machine. The convergence criterion for the EM algorithm was set to 0.001.

Table 1: Average computing times [s] and number of iterations of the original detector (center columns) and average computing time [s] for the accelerated detector (rightmost column).

ω^{-1}	$K = 1$		$K = 2$		$K = 3$		fast
0.75	6.0 s	11.1	20.2 s	13.3	52.9 s	13.9	0.1 s
orig.	7.6 s	14.4	19.9 s	13.4	45.8 s	12.8	0.1 s
1.5	6.5 s	6.5	16.8 s	11.2	38.6 s	10.7	0.1 s